This article has been published in Metallurgical and Materials Transactions B. The final publication is available at Springer via https://doi.org/10.1007/s11663-015-0387-x .

A multi-scale thermomechanical-solidification model to simulate the transient force field deforming an aluminum 6061 semisolid weld

H.R. Zareie Rajani*, A.B. Phillion
School of Engineering, The University of British Columbia, Kelowna, BC, Canada
*hamid.zareie.rajani@ubc.ca

Abstract

Formation of hot cracks is strongly affected by the transient force field acting on the semisolid weld-base metal interface. This paper presents a model that numerically simulates such a transient force field as a function of welding parameters. The model consists of two modules: 1) By means of a granular model of solidification, the microstructure of the semisolid area within the weld is reconstructed in three dimensions; 2) Since the transient force field is developed through the mechanical interaction between the semisolid weld and its base metal, the mechanical response of the base metal to the solidification of the weld is then simulated through finite element analysis. The results show that changing welding parameters and welding constraints varies the transient force field. Based on the obtained force fields, a qualitative study is also conducted to predict the susceptibility of various welds to hot cracking.

Keywords: Welding; Solidification; Semi-solid; Multiscale modelling.

1 Introduction

Fusion welding is a joining process that uses solidification of the base metal and sometimes a filler metal to make the weld. In aluminum alloy welding, a major defect that can arise is hot cracking [1] in which an intergranular crack forms during the terminal stages of solidification. A hot crack forms within the two-phase mushy zone behind the weld pool, rupturing liquid films that are present at grain boundaries.

Hot cracking occurs due to the combination of limited intergranular liquid flow in response to solidification shrinkage, and semisolid deformation caused by thermal contraction and mechanical constraints [2, 3]. To date, various mechanisms have been proposed to predict the formation of this defect [3, 4]. As shown in early work by Pellini [5] and later Magnin [6], hot cracking in castings can be related to the total strain accumulated in the semisolid. Other researchers [7, 8] have shown that high strain rates seem to hinder the accommodation of deformation within the semisolid material, and consequently fracture occurs. Based on these findings, several strain and strain rate - based criteria have been developed to qualitatively predict hot crack formation [2,7-12,14] in both casting and welding.

Although the actual strain and strain rate fields within a semisolid weld are position and time dependent, existing hot cracking criteria use an averaged value across the semisolid weld to assess crack susceptibility [2, 14]. Such a simplifying assumption limits the application of hot cracking criteria, as they are not able to predict the position and size of this defect [3] for a given set of welding parameters. This assumption is nonetheless used due to the challenge of obtaining the non-uniform strain and strain rate fields within the semisolid during welding. Experimentally, it is quite difficult to obtain the transient strain field due to the short lifetime of the weld pool and the high temperature conditions. Numerical models, in contrast, are able to predict this behaviour as they are not limited by time and temperature, but are complex due to the two-phase nature of semisolids and the interaction between the semisolid weld and the base metal.

In order to simulate the transient strain fields during welding [15], a model must first take into account the shape of the weld domain and then couple the resulting mesh with the force field $\vec{f}_{\text{total}}$ that causes deformation. Considering the semisolid weld as the simulation domain, the first step requires a mesh matching the microstructure of the weld fusion zone, while the second step requires

detailed knowledge of the force field that deforms the semisolid weld. This total force field consists of the external forces that act on the boundaries of the semisolid weld, $\vec{f}_{\partial\Omega_{\text{fusion|semisolid weld}}}$, and the internal forces resulting from thermal contraction and solidification shrinkage, $\vec{f}_{\Omega}$, *i.e.*, $\vec{f}_{\text{total}} = \vec{f}_{\partial\Omega_{\text{fusion|semisolid weld}}} + \vec{f}_{\Omega}$. The internal forces can be easily defined for the solidifying grains as a function of temperature and solid fraction [2, 3]. On the other hand, determining the external force field is complicated as it results from mechanical interaction between the semisolid weld and the base metal in response to the non-uniform thermal expansion and contraction of the weld pool and adjacent base metal during the welding process. Additionally, the domain must be large enough to capture both the stochastic effects due to variations in grain morphology, and the solid-liquid interactions on the interface between the base metal and the semisolid weld called the fusion surface.

Recently, a number of studies have been carried out to simulate the microstructure of the semisolid weld at the meso scale. Zhong et al. [16] and Bordreuil et al. [17] have used cellular automaton (CA) methods to reconstruct in both 2-D and 3-D the microstructure of the weld directly after solidification. Zareie Rajani et al. [18, 19] used a multi-scale model based on a method proposed by Mathier [20] to reconstruct in 3-D the evolving semisolid composed of solidifying grains and micro liquid channels. Unlike the first step, the second step, i.e. determining the external force field acting on the semisolid weld, has received limited research. As stated by Służalec [21], thermomechanical studies in welding mainly focus on residual stresses, not on the external forces acting on the semisolid weld. Residual stresses evolve over a relatively long period of time when the fully solidified weld has cooling down. As a result, these studies have ignored the mechanical response of the base metal to the weld solidification [22]. Consequently, there is currently little knowledge of the transient external forces acting on the semisolid weld.

In this study, a numerical method is presented for performing a transient thermomechanical analysis of the interaction between the semisolid weld and its base metal for the aluminum alloy AA6061 during tungsten inert gas welding. The analysis is carried out on a domain consisting of the base metal only; the influence of the semisolid weld is captured through definition of boundary conditions. The research results help to explain the behaviour of the weld at the interface between the base metal and the semisolid weld, and provide as an output the interfacial reaction forces that can deform the semisolid weld, leading to hot cracking. The effect of welding parameters including amperage, welding speed, and welding constraints on the interfacial reaction forces are examined and discussed.

2 Description of the model

2.1. Overview

Fig. 1 illustrates the structure of the multi-scale thermomechanical model developed to determine the mechanical forces acting on the interface between the base metal and the semisolid weld, called the fusion surface. The model combines purpose-written C++ code with the commercial Abaqus finite element software. As can be seen, five major modules are embedded within this model. (1) The Input Data module contains the welding parameters, material properties, and model definitions. (2) The Geometry module generates the mesh and boundary conditions for performing the mechanical analysis based on the welding parameters. (3) The Thermal Analysis module outputs the temperature field in the base metal as a function of welding parameters. (4) The Solidification module [18-19] reconstructs the semisolid weld microstructure based on the welding parameters and then outputs the shrinkage displacement on the fusion surface, which will act as a Dirichlet boundary condition for the base metal. (5) The Base Metal Deformation module links the

Solidification, Geometry, and Thermal Analysis modules in order to calculate the reaction force field on the fusion surface of the base metal ($\vec{f}^{\text{reaction}}_{\partial\Omega_{\text{fusion|base metal}}}$). Specifically, a PYTHON script output from the Geometry module is used to perform the mechanical simulation on the base metal via Abaqus, while the shrinkage displacement acting on the fusion surface and predefined temperature fields applied to the simulation domain are set using outputs of the solidification and thermal analysis modules. Since the amount of plastic strain within the base metal is small [14], the mechanical model is sequentially coupled to the thermal model instead of solving a fully coupled thermomechanical problem. Utilizing Newton's third law of motion, the external force field acting on the semisolid weld during welding ($\vec{f}_{\partial\Omega_{\text{fusion|semisolid weld}}}$) is then calculated as:

$$\vec{f}_{\partial\Omega_{\text{fusion|semisolid weld}}} = -\vec{f}^{\text{reaction}}_{\partial\Omega_{\text{fusion|base metal}}} \quad (1)$$

2.2. Input Module

This module contains all of the input data required to perform the thermomechanical simulation, including the model parameters and constants for each of the remaining modules, the welding procedure (applied amperage, welding speed and constraints on the base metal), and the constitutive behaviour of the base metal.

During welding, the base metal experiences large variations in temperature. Thus, the model assumes that material properties are temperature-dependent. The temperature-dependent flow stresses [23, 24] for AA6061, shown in Fig. 2 at a constant strain rate of 0.001 s^{-1}, are assumed to follow an elastic-plastic constitutive law with work hardening obeying the von Mises' plasticity criterion, *i.e.* $\sigma_{\text{o}}|_T = F(\varepsilon^{\text{pl}}_{\text{eq}})|_T$, where $\sigma_{\text{o}}|_T$ denotes a temperature-dependent flow stress and $\varepsilon^{\text{pl}}_{\text{eq}}$ is the equivalent plastic strain. Since welding parameters do not significantly change the strain rate

of the base metal [22] and also due to the relatively low sensitivity of AA6061 to strain rate [24-26], strain rate dependency is not included. Note that Abaqus uses linear interpolation to calculate constitutive properties at temperatures other than the ones given in Fig. 2.

2.3. Geometry (and Boundary Conditions) module

The 3D simulation domain (Ω) for the mechanical analysis consists of the base metal itself with a small portion removed representing the semisolid weld line. Due to symmetry, only one-half of the weld, and only one side of the base metal are included in the domain. As illustrated in Fig. 3a, the base metal is separated from its surroundings via a boundary ($\partial\Omega$) composed of seven different surfaces: a parabolic fusion surface ($\partial\Omega_{\text{fusion|base metal}}$) representing the contact between the base metal and the weld line; a symmetry surface ($\partial\Omega_{\text{symmetry}}$) lying on the symmetry plane of the weld below the fusion surface; the back surface ($\partial\Omega_{\text{back}}$) that is assumed to be either free or constrained; and four free surfaces ($\partial\Omega_{\text{free}}$) that are not in contact with anything but the air. Based on the defined Cartesian coordinate system, the depth and width of the plate respectively lie along the *X* and *Y* directions, and the *Z* direction follows the line of welding. The width and thickness of the base metal are assumed to be 50 mm and 3 mm, and the simulated weld length is set at 20 mm. The shape of the material removed representing the weld pool is given by the welding procedure, and was determined experimentally [18]. As shown in Fig. 3b, the choice of welding parameter can significantly influence the geometry of the fusion surface.

Once defined, the simulation domain is then discretized using a mesh composed of 8-node linear elements that vary in size depending on their position relative to the fusion surface. Fig. 3c depicts a 2D cross-section of the discretized domain. The area far from the weld surface, labeled A, contains elements with a gradient in average size from 1000 to 300 μm. The refined area near the

weld surface, labeled B, contains elements varying in size from 300 to 100 μm. The need for a 3D simulation domain is demonstrated in Fig. 4, which shows a portion of the base metal and the fusion zone. As can be seen, the fusion zone is composed of three different areas along the weld line: the molten metal pool (represented by empty space); the semisolid weld forming right behind the molten metal; and finally the fully solidified weld. As the process is transient, and the welding torch is moving, each element on the fusion surface will first be in contact with the molten aluminum, then the semisolid weld, and finally the fully solidified metal. Note that the solid region in front of the molten metal pool is ignored as the model focuses on only the mechanical interaction between the fusion zone and the base metal.

The boundary conditions applied to the different surfaces are as follows:

(1) $\partial\Omega_{\text{free}}$ – As the free surfaces (four) are only in contact with air, a homogeneous boundary condition, $\vec{f}|_{\partial\Omega_{\text{free}}} = 0$, is defined.

(2) $\partial\Omega_{\text{symmetry}}$ – This surface is constrained in the Y direction due to symmetry, and also in X and Z directions since the weld line is normally clamped to prevent misalignment defects during welding.

(3) $\partial\Omega_{\text{back}}$ – The back surface can be subject to different displacement boundary conditions, $\vec{U}|_{\partial\Omega_{\text{back}}} = \vec{U}_{\text{o}}$, where $\vec{U}$ is the material flow, to model various welding constraints including clamped ($\vec{U}_{\text{o}} = 0$), and tension/compression ($\vec{U}_{\text{o}} \neq 0$). It is also possible to assume that the back surface of the base metal is not clamped during welding by setting a homogenous boundary condition, $\vec{f}|_{\partial\Omega_{\text{back}}} = 0$.

(4) $\partial\Omega_{\text{fusion|base metal}}$ – The boundary condition applied to the fusion surface of the base metal is complex since the displacement field, $\vec{U}|_{\partial\Omega_{\text{fusion}}} = \vec{D}_{(\vec{x},t)}$ is imposed by the shrinkage

associated with solidification rather than a mechanical tool such as a clamp. Due to the solidification conditions occurring during welding, the resulting shrinkage-related displacements are non-uniform across this interface and vary with time. This boundary condition will be further explored in Section 2.5.

The output of the Geometry module is a Python script containing the meshed simulation domain and the boundary conditions needed for the mechanical analysis.

2.4. Thermal Analysis module

Simulation of the response of the base metal to a welding procedure requires knowledge of the thermal fields in order include the effects of thermal expansion and contraction during the welding process, and to properly account for the variation in flow stress with temperature resulting from the thermal gradient. The thermal field, T, during welding as a function of spatial coordinates R (radial distance from the centre of the weld), and X (distance from the centre of the weld along the weld line) can be calculated from the Rosenthal equation [14, 27],

$$\frac{2\pi(T - T_o)KR}{Q} = exp\left[\frac{-V(R - X)}{2\alpha}\right] \quad (2)$$

where T_o is the initial temperature of the workpiece, V is the travel speed of the torch, Q is the heat transferred from the torch to the metal, and K and α are the thermal conductivity and diffusivity of the base metal. In the present model, the temperature evolution throughout the base metal was calculated from the Rosenthal equation for a given set of welding parameters using a Matlab script within the Thermal Analysis module. Fig. 5 depicts the obtained temperature field within the base metal for a weld fabricated with a speed of 3 mm/s and a current of 120 A. The image shows the point when the fusion zone is molten only at the front edge of the weld pool. The remainder of the

fusion surface sees temperatures in the semisolid regime. Utilizing the obtained temperature fields, this module generates the subroutine UTEMP through which the time-dependent temperature distribution during welding is assigned.

2.5. Solidification module

2.5.1. Necessity of performing a solidification analysis

In order to study the mechanical response of the AA6061 base metal to the forces arising during solidification of the weld pool, it is necessary to apply boundary conditions that represent the interaction between the base metal and its surroundings as outlined in section 2.3. The boundary condition applied to the fusion surface, related to the solidification shrinkage, varies with position and time depending on the solidification kinetics of the weld pool. Thus, the weld pool solidification must be simulated.

2.5.2. Meso-scale solidification model

The Solidification module uses the model of Zareie Rajani et al. [18] to simulate solidification of the weld pool at the meso-scale. This model is composed of both columnar and equiaxed solid grains and also a network of micro liquid channels spread between each grain; the fully solid microstructure is generated from a series of Voronoi tessellations performed on different regions in space. Solidification in each grain is simulated by combining an evolving temperature field within the weld pool generated by the Rosenthal equation with a fraction solid curve for AA6061 generated by Thermocalc. Fig. 6 shows the semi-solid weld structure at different times during the welding process. The model predicts the evolving microstructure morphology and transitions within the semisolid material during the welding process. These characteristics vary as a function of welding parameters.

2.5.3. Calculation of displacements on the fusion surface related to solidification shrinkage

Considering the Cartesian coordinate system in Fig. 3, the total solidification shrinkage in the weld pool can be described as a deformation in the three primary directions *X*, *Y*, and Z. In the *X* and *Z* directions, it is assumed that the shrinkage is fully accommodated by displacement of a free end. In the case of *X*, the free end is the air/weld pool interface. In the case of *Z*, the free end is the fully liquid molten metal just below the weld torch. Such an assumption is justified by the observation of a concave surface seen at the top of a weld when filler metal is not used to compensate for shrinkage [14]. On the other hand, the fusion surface and the rigid symmetry plane at the centre of the weld line confine material flow in the *Y* direction. This confinement results in the application of a force on the fusion surface to accommodate the shrinkage component in *Y* direction, *i.e.* lateral solidification contraction.

Based on conservation of mass, the lateral solidification contraction Y_{Sh} for a confined domain within the semisolid weld can be expressed as:

$$Y_{Sh} = Y_o \sqrt[3]{g_s}(1-\alpha) \tag{3}$$

where $\alpha = \sqrt[3]{\rho_l/\rho_s}$ is the linear shrinkage coefficient, ρ_l and ρ_s are the liquid and solid densities respectively, and Y_o and g_s denote the lateral length and volumetric solid fraction. For a small solidification increment, equation (3) can be rewritten in differential form:

$$dY_{Sh} = \frac{1}{3} Y_o (1-\alpha) g_s^{-\frac{2}{3}} dg_s \tag{4}$$

Integration of equation (4) yields the gradual, accumulation of the lateral solidification contraction within the confined space as a function of solid fraction. Since the semisolid is not able to transfer stress before a continuous solid bridge forms across the confined domain, *i.e.* the percolation point

or mechanical coalescence, the integration domain is limited to values of solid fraction at which the semisolid is percolated, *i.e.*:

$$Y_{\mathrm{Sh}}|_t = \int_{g_{\mathrm{s}}|_{\mathrm{p}}}^{g_{\mathrm{s}}|_t} \frac{1}{3} Y_{\mathrm{o}}(1-\alpha) g_{\mathrm{s}}{}^{-\frac{2}{3}} dg_{\mathrm{s}} = Y_{\mathrm{o}}(1-\alpha)(\sqrt[3]{g_{\mathrm{s}}|_t} - \sqrt[3]{g_{\mathrm{s}}|_{\mathrm{p}}}) \quad (5)$$

In equation (5), $\mathrm{Y_{Sh}}|_{\mathrm{t}}$ represents the evolution in linear solidification contraction with time, $\mathrm{g_s}|_{\mathrm{t}}$ denotes the average solid fraction of the confined space as a function of time, and $\mathrm{g_s}|_{\mathrm{p}}$ represents the average solid fraction at the percolation point, assumed to occur at a value of $\mathrm{g_s}$ =0.95. The confined elements used in this study are shown in Fig. 7. These elements, given the name bar elements, lie along the Y direction connecting the weld center to the fusion surface. The ensemble of the bar elements and their corresponding displacement functions ($\mathrm{Y_{sh}}|_t{}^i$), where the index *i* represents an individual bar element, yields the Dirichlet boundary condition acting on the fusion surface:

$$\vec{U}|_{\partial\Omega_{\mathrm{fusion|base\ metal}}} = \vec{D}_{(\vec{x},t)} = \begin{cases} D_Y|_t = Y_{\mathrm{sh}}|_t{}^i \\ D_X|_t = D_Z|_t = 0 \end{cases}, \qquad \vec{x} \in A_Y{}^i \quad (6)$$

where the term $A_Y{}^i$ refers to the projection of bar element *i* onto the portion of the fusion surface containing the given point in $\vec{D}_{(\vec{x},t)}$. In order to obtain $g_{\mathrm{s}}|_t{}^i$, the thermomechanical analysis module is linked to the solidification module. The solidification module provides the average solid fraction of the bar elements during welding, and therefore, enables the model to define a proper time and position -dependent boundary condition on the fusion surface of the base metal. Note that the semisolid weld is assumed to remain intact during solidification.

The shrinkage displacement values, $\vec{D}_{(\vec{x},t)}$, at three different points on the fusion surface of a weld fabricated using a welding current of 120 A and a welding speed of 3 mm/s are plotted as a function of welding time in Fig. 8. In this figure, the welding time of zero represents the beginning of solidification in the domain. As the three points are at different locations on the fusion surface,

they start to displace at different times. Each also accumulates different amounts of shrinkage displacement since the percolation through the semisolid weld does not occur uniformly, and the size of the bar elements is different at each location. The bar element A is the largest, and thus, it experiences the largest displacement.

2.6. Base Metal Deformation module

The Base Metal Deformation module performs a static mechanical analysis on the base metal using the Abaqus finite element code in order to obtain the reaction forces acting on the fusion surface, $\vec{f}^{\text{reaction}}_{\partial\Omega_{\text{fusion|base metal}}}$. This module receives as input the geometry and boundary conditions (Geometry module), the evolution in temperature with time throughout the domain (Thermal Analysis module), and the displacement along the fusion surface (Solidification module). equation (1) is then applied to extract the transient force field that deforms the semisolid weld, *i.e.* $\vec{f}_{\partial\Omega_{\text{fusion|semisolid weld}}}$.

3 Results and discussion

3.1. Quantitative analysis

Since the deformation of the semisolid weld is dominated by lateral stresses [14, 21, 22], *i.e.* the stresses normal to the weld line, the quantitative analysis focuses on the *Y* components of the simulated force field. Fig. 9a shows the lateral components of the calculated force field acting on the fusion surface of a small section of the semisolid weld at welding time of t=1.8 s. The weld is fabricated on an unclamped aluminum 6061 plate using a welding current of 120 A and a welding speed of 3 mm/s. Welding time of zero is assumed to be the time at which solidification begins in this section. Also, note that positive force values represent tensile lateral forces, while negative

force values are associated with compressive lateral forces. Since the calculated force fields are closely linked to the solidification behaviour of the semisolid weld, the distribution of the solid fraction of the bar elements (g_s) is also plotted over the fusion surface in Fig. 9b.

Based on the obtained results, the transient external force field has a complex nature where both tensile and compressive force components simultaneously act on the semisolid weld. Such behaviour can be linked to a complex nature of deformation within the base metal, where nonuniform transient thermal stresses combine with transient solidification contraction to control the material flow. As discussed in section 1, by applying the obtained force fields on the fusion surface (e.g. Fig. 9a) as natural boundary conditions to the semisolid weld, one could quantitatively model the deformation in the fusion zone, and thus acquire the actual strain field of the semisolid weld.

3.2. Qualitative analysis

The obtained results can be also used to qualitatively assess the susceptibility of the weld to hot cracking. To do so, the tensile force components in *Y* that apply on bar elements with $g_s > g_s|_p$ are averaged and then divided by the percolated area of the fusion surface to obtain the average tensile stress acting on the semisolid weld. In order to gain insight into hot crack susceptibility, the average tensile stress values are then compared against known critical tensile stress values from the literature. A recent experimental study by Giraud et al. [28] showed that the percolated semisolid AA 6061 cannot bear tensile stresses greater than 5 MPa. This value is considered as the critical criterion for defect formation and thus average tensile stresses greater than 5 MPa are assumed to cause excessive deformation and consequently initiate defects.

The calculated average tensile stresses acting on the fusion surface of clamped AA 6061 semisolid welds as a function of time fabricated by various welding parameters are shown in Fig. 10 for different welding speeds between 2 and 5 mm/s. The results indicate that at a constant welding speed, increasing the welding current generates larger average tensile stresses. In other words, using higher welding currents at a fixed welding speed will increase the risk of sever deformation within the semisolid weld, and will make the weld more susceptible to hot cracking. Such an observation can be explained through the shrinkage displacement. By increasing the welding current, larger welds form, leading to larger amounts of solidification contraction, as given by equation (3). Higher magnitudes of shrinkage contraction will then create larger reaction forces on the fusion surface. This result qualitatively matches prior experimental studies [14], where it was shown that high welding current and large weld pools increase the risk of hot cracking.

Fig. 10 indicates that the welding speed also affects the average tensile stress deforming the semisolid weld. Such as shown in Fig. 10a, at a low welding speed of 2 mm/s, the maximum average tensile stress is relatively low. However, once the welding speed increases to 3 and 4 mm/s, the maximum average tensile stress significantly rises (Figs. 10b and c). Fig. 10d suggests that such an ascending behaviour does not last over high welding velocities where the maximum average tensile stress drops at a welding speed of 5 mm/s. In other words, the results show that the maximum average tensile stress and consequently the susceptibility to hot cracking are higher at a medium range of welding velocity. This result can be explained through the interaction between two main parameters that control the material flow within the base metal: 1) solidification shrinkage causing material flow within the base metal since larger welds are accompanied by more lateral solidification contraction and consequently bigger driving forces for the materials flow, and 2) the amount of resistance against material flow that strongly depends on the temperature of the

base metal since colder base metals are accompanied by higher elastic moduli and larger yield strengths. High temperature conditions soften the base metal and lower the amount of resistance. As a result of Newton's third law of motion, cold base metals and large welds generate high magnitudes of reaction forces, while hot base metals and smaller welds create lower magnitudes of reaction forces. Therefore, the small average tensile stresses observed at low welding speeds can be linked to the excessive softness of the base metal that stems from high temperature conditions during slow welding. By increasing the welding speed, the heat input decreases leading to a colder base metal. As a result, the reaction force and consequently the average tensile stress deforming the semisolid weld increase. Although the base metal is coldest at high welding velocities, the reaction forces do not keep growing since there is a significant drop in the size of the weld. In this simulation, by increasing the welding speed from 4 mm/s to 5 m/s at a constant welding current of 120 A, the depth of weld penetration decreased from 2 mm to 1 mm. It is hypothesized that very small welds do not generate enough linear solidification contraction to maintain the ascending trend of the reaction forces.

The obtained average tensile stresses shown in Fig. 10 can also be translated into average tensile strain rates using a constitutive equation for semisolid aluminum alloys [29]. Fig. 11 shows the variation of the average tensile strain rate during welding of a clamped plate for a welding speed of 5 mm/s and three different welding currents. The outcomes suggest that the average tensile strain rate rapidly rises once the semisolid weld is percolated. However, as the rigidity of the semisolid structure increases at high solid fractions, the growth rate of the average tensile strain rate decreases. Furthermore, the maximum average tensile strain rate increases with an increase in the welding current. This observation can be linked to the fact that higher welding currents amplify the average tensile stress acting on the semisolid weld (Fig. 10d).

Another welding parameter that is well known to affect the susceptibility of the weld to hot cracking is the constraining condition of the weld [14]. Hence, the developed model is also utilized to investigate how welding constraints change the external force field deforming the semisolid weld. To do so, five different constraining conditions are simulated by applying different Dirichlet boundary conditions to the back surface of the plate welded by a welding speed of 3mm/s and a welding current of 120 A. In the first, the back surface of the plate was clamped ($\vec{U}_o = 0$). In the rest, the back surface was displaced in tension along the *Y* direction. The displacement was initiated at the time corresponding to the time that at least one of the bar elements within the semisolid weld had percolated. The displacement reached the maximum value, 10, 20, 30, 50 μm and 100 μm, when the weld had fully solidified. Such as shown in Fig. 12, applying tensile stresses to the plate during welding results in the average tensile stresses along the fusion surface approaching and exceeding the critical value, making the weld severely susceptible to defect formation. This result can be verified by experimental studies showing the destructive effect of welding constraints on hot cracking [3, 14]. According to the obtained results, the model suggests that tensile lateral displacements greater than 10 μm most likely initiate solidification defects within the semisolid weld as they result in average tensile stresses greater than the assumed critical value of 5 MPa.

4 Conclusions

The present study couples a mesoscale solidification model of welding with a thermomechanical model of the base metal in order to investigate deformation within the semisolid weld as a function of welding parameters. The model considers solidification contractions as well as the temperature-dependent stress response of the base metal during welding to yield the force field acting on the fusion surface of the aluminum alloy AA6061 during tungsten inert gas welding. Based on the obtained results, for a plate 3 mm in thickness, the semisolid weld experiences the maximum

deformations at a moderate welding speed of 4 mm/s and a high level of welding current. The results also suggest that any external tensile stress during welding will amplify the deformation of the semisolid weld. In a future study, the obtained force fields on the fusion surface will be coupled with a deformation model of the semisolid weld in order to study hot cracking and other local welding phenomena in which deformation plays a key role.

Acknowledgment

The authors wish to thank the American Welding Society (AWS), Rio Tinto Alcan, and the Natural Sciences and Engineering Research Council of Canada (NSERC) for financial support.

References

[1] D. Dye, O. Hunziker, R. C. Reed: Acta Mater., 2001, **49**, pp. 683-697.

[2] N. Coniglio, C. E. Cross: Int. Mater. Rev., 2013, **58**, pp. 375-397.

[3] L. Katgerman, D. J. Eskin: 'In search of the prediction of hot cracking in aluminum alloys', In: C. Lippold, B. Herold, editors: 'Hot cracking phenomena in welds II', pp. 3-18, 2008, Springer, Berlin.

[4] D. J. Eskin, Suyitno, L. Katgerman: Prog. Mater. Sci., 2004, **49**, pp. 629-711.

[5] W. S. Pellini: J. Foundry, 1952, **80**, pp. 124-133.

[6] B. Magnin, L. Maenner, L. Katgerman, S. Engler: Mater. Sci. Forum, 1996, **217-222**, pp. 1209-1214.

[7] N. N. Prokhorov: Russ. Castings Production, 1962, **2**, pp. 172-175.

[8] M. Rappaz, J. M. Drezet, M. Gremaud: Metall. Mater. Trans. A, 1999, **30A**, pp. 449-455.

[9] J. C. Borland: Weld. Met. Fabr., 1979, **47**, pp. 99-107.

[10] T. Senda, F. Matsuda, G. Takano: J. Jpn. Weld. Soc., 1973, **42**, pp. 48-56.

[11] K. Nakata, F. Matsuda: Trans. JWRI, 1995, **24**, pp. 83-94.

[12] I. I. Novikov, O. E. Grushko: Mater. Sci. Technol., 1995, **11**, pp. 926-932.

[13] J. M. Drezet, D. Allehaux: 'Application of the Rappaz Drezet Gremaud hot tearing criterion to welding of aluminum alloys', In: C. Lippold, B. Herold, editors: 'Hot cracking phenomena in welds II', pp. 19-38, 2008, Berlin, Springer.

[14] S. Kou: 'Welding metallurgy', 2003, John Wiley & Sons Inc, New Jersey.

[15] M. Rappaz, M. Bellet, M. Deville: 'Numerical modelling in materials science and engineering', 2003, Springer, New York.

[16] X. H. Zhong, Z. B. Dong, Y. H. Wei, R. Ma: J. Cryst. Growth, 2009, **311**, pp. 4778-4783.

[17] C. Bordreuil, A. Niel: Comp. Mater. Sci., 2014, **82**, pp. 442-450.

[18] H. R. Zareie Rajani, A. B. Phillion: Acta Mater., 2014, **77**, pp. 162-172.

[19] H. R. Zareie Rajani, A. B. Phillion: Mater. Sci. Forum, 2014, pp. **790**, 79-84.

[20] V. Mathier, A. Jacot, M. Rappaz: Mater. Sci. Eng., 2004, **12**, pp. 479-490.

[21] A. Służalec: 'Theory of thermomechanical processes in welding', 2005, Springer, Dordrecht, The Netherlands.

[22] L. E. Lindgren: 'Computational welding mechanics: thermomechanical and microstructural simulations', 2007, CRC Press, New York.

[23] Y. V. R. K. Prassad, S. Sasidhara, H. L. Gegel, J. C. Malas: 'Hot working guide: A compendium of processing maps', 1997, ASM International, Ohio.

[24] S. Mahabunphachai, M. Koç: Mater. & Design, 2010, **31**, pp. 2422-2434.

[25] L. Woei-Shyan, T. Zih-Chao: Mater. & Design, 2014, **58**, pp. 116-124.

[26] A. Manes, L. Peroni, M. Scapin, M. Giglio: Procedia Engineering, 2011, **10**, pp. 3477-3482.

[27] H. R. Zareie Rajani, H. Torkamani, M. Sharbati, S. H. Raygan: Mater. & Design, 2012, **34**, pp. 51-57.

[28] E. Giraud, M. Suery, M. Coret: Metall. Mater. Trans. A, 2010, **41A**, pp. 2257-2268.

[29] A. B. Phillion, S. L. Cockcroft, P. D. Lee: Model. Simul. Mater. Sci. Eng., 2009, **17**, pp. 1-15.

Figure Captions

Fig. 1. The structure of the multi-scale thermomechanical model.

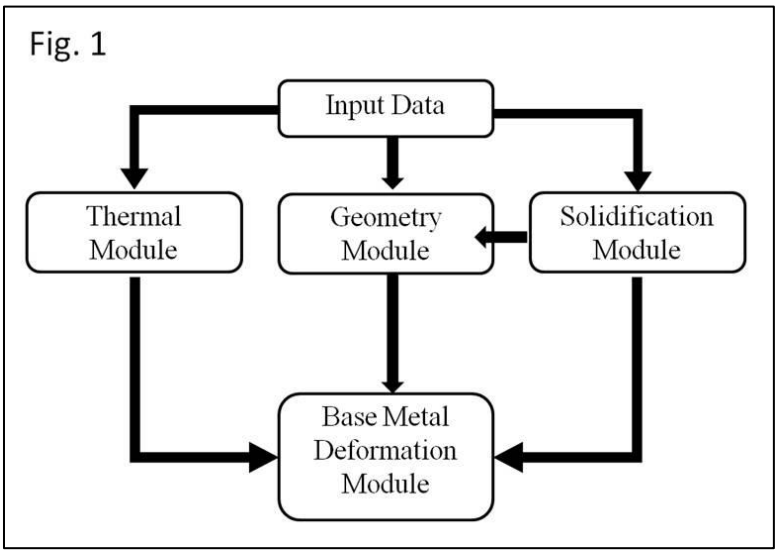

Fig. 2. The temperature-dependent flow stresses for AA6061 [23, 24].

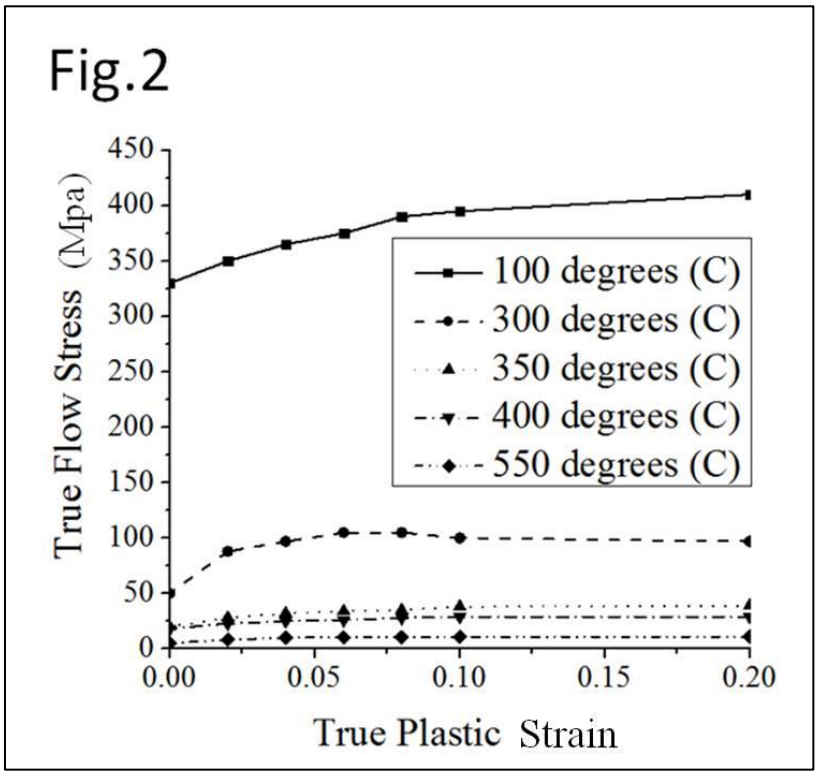

Fig. 3. (a) The boundaries of the base metal; (b) Variation in the size of the weld and consequently the shape and size of the base metal geometry due to using different welding parameters; (c) The discretized base metal in 2D.

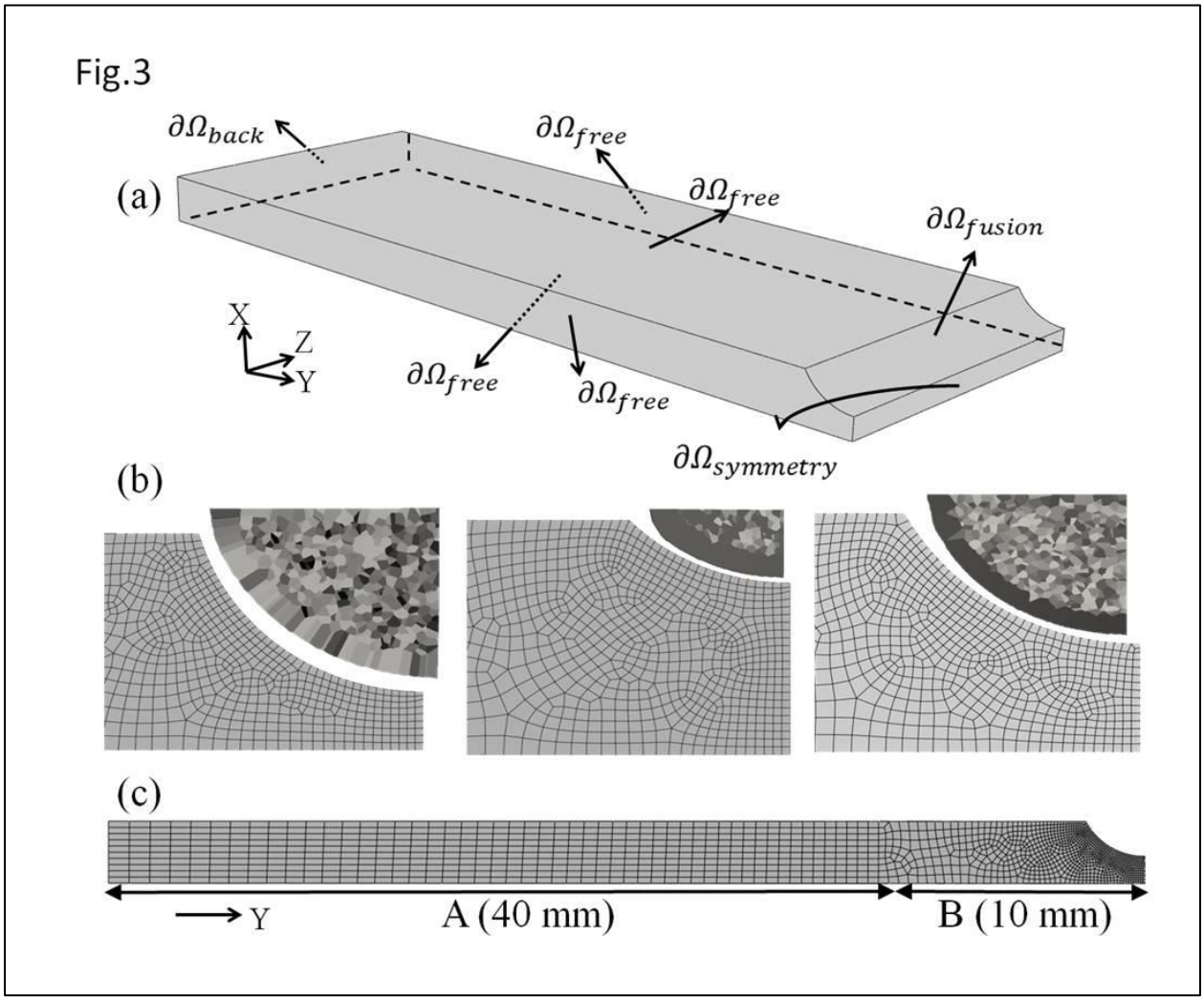

Fig. 4. Various transient regions on the fusion surface separating the base metal from the weld line.

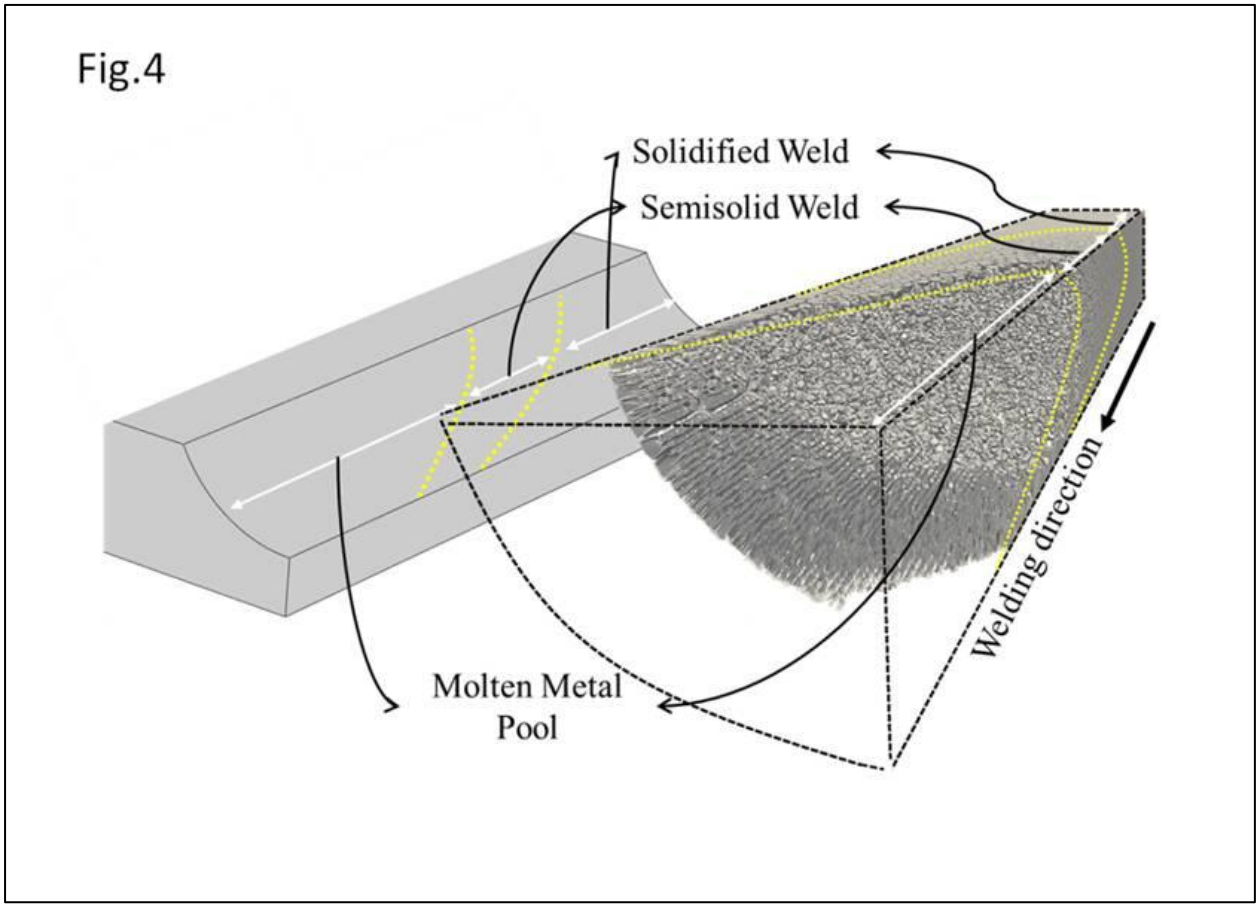

Fig. 5. The temperature field within the base metal for a weld fabricated with a speed of 3 mm/s and a current of 120 A.

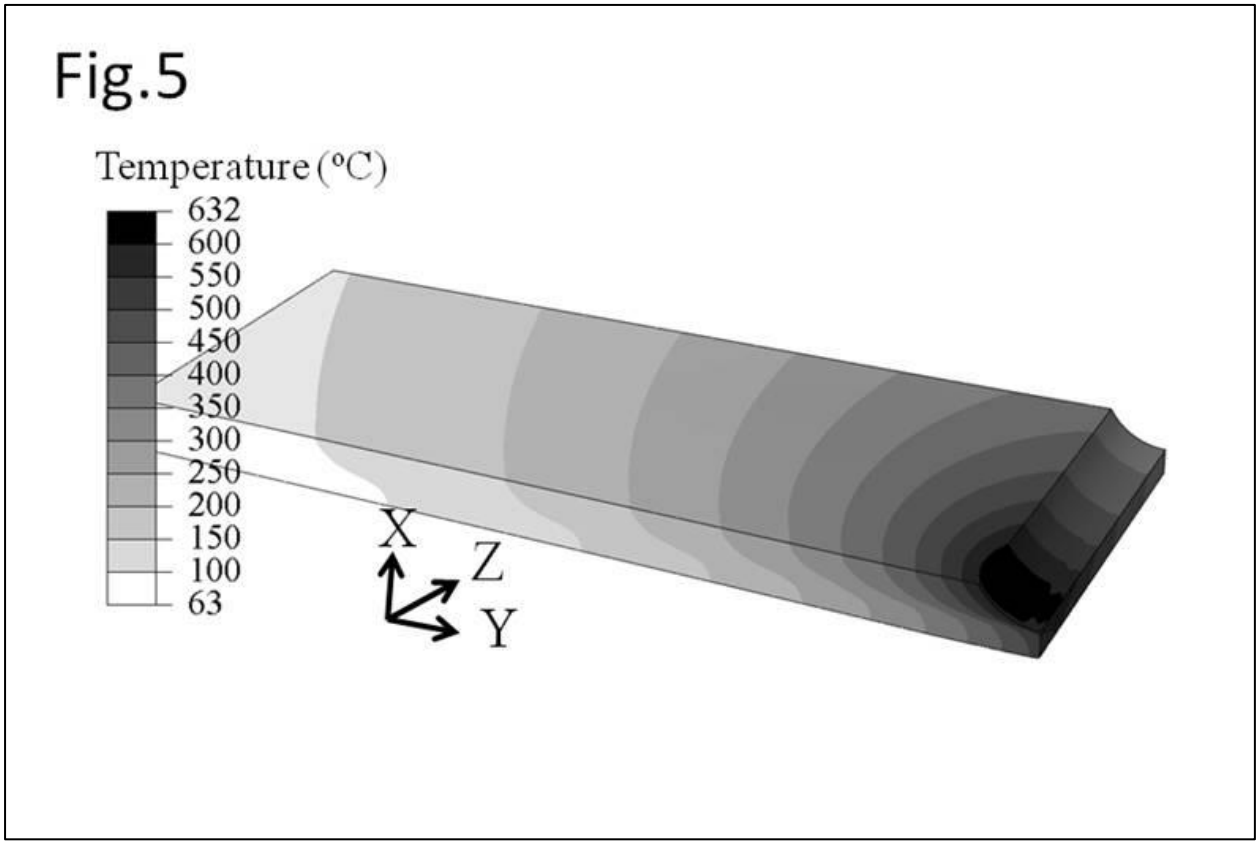

Fig. 6. The developed microstructure of a semisolid weld fabricated by welding speed of 3 mm/s and welding current of 120 A at welding time of (a) t=0.2 s, (b) t=0.4 s, and (c) t=0.8 s.

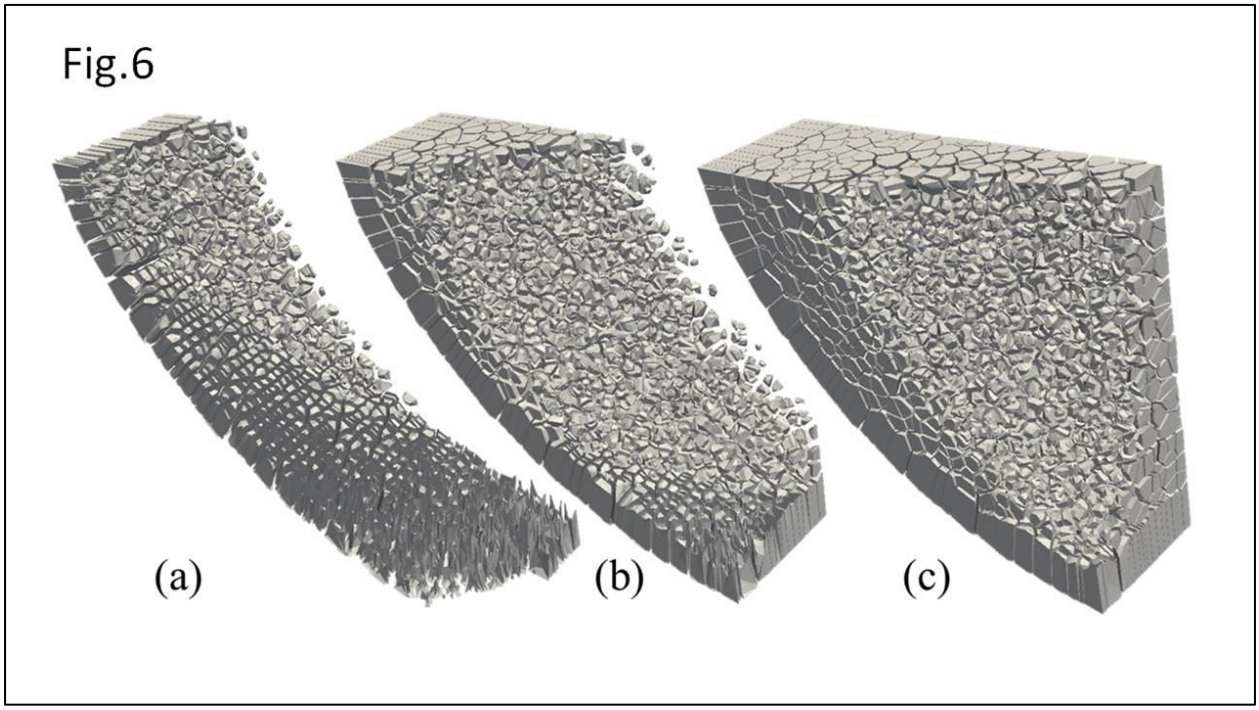

Fig. 7. The bar elements used to obtain the local solid fraction within the semisolid weld.

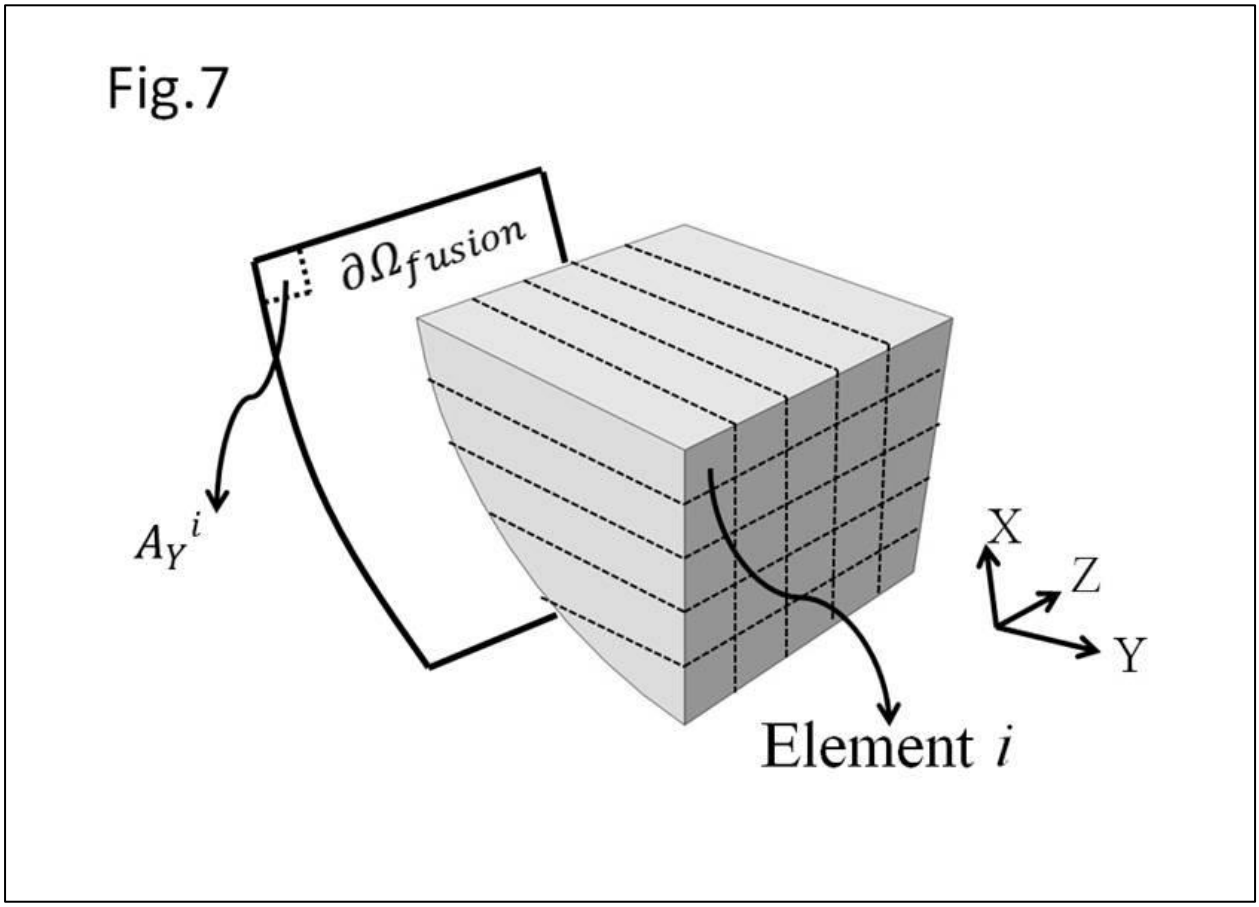

Fig. 8. The shrinkage displacement values, $\vec{D}_{(\vec{x},t)}$, at three different points on the fusion surface of a weld fabricated using a welding current of 120 A and a welding speed of 3 mm/s.

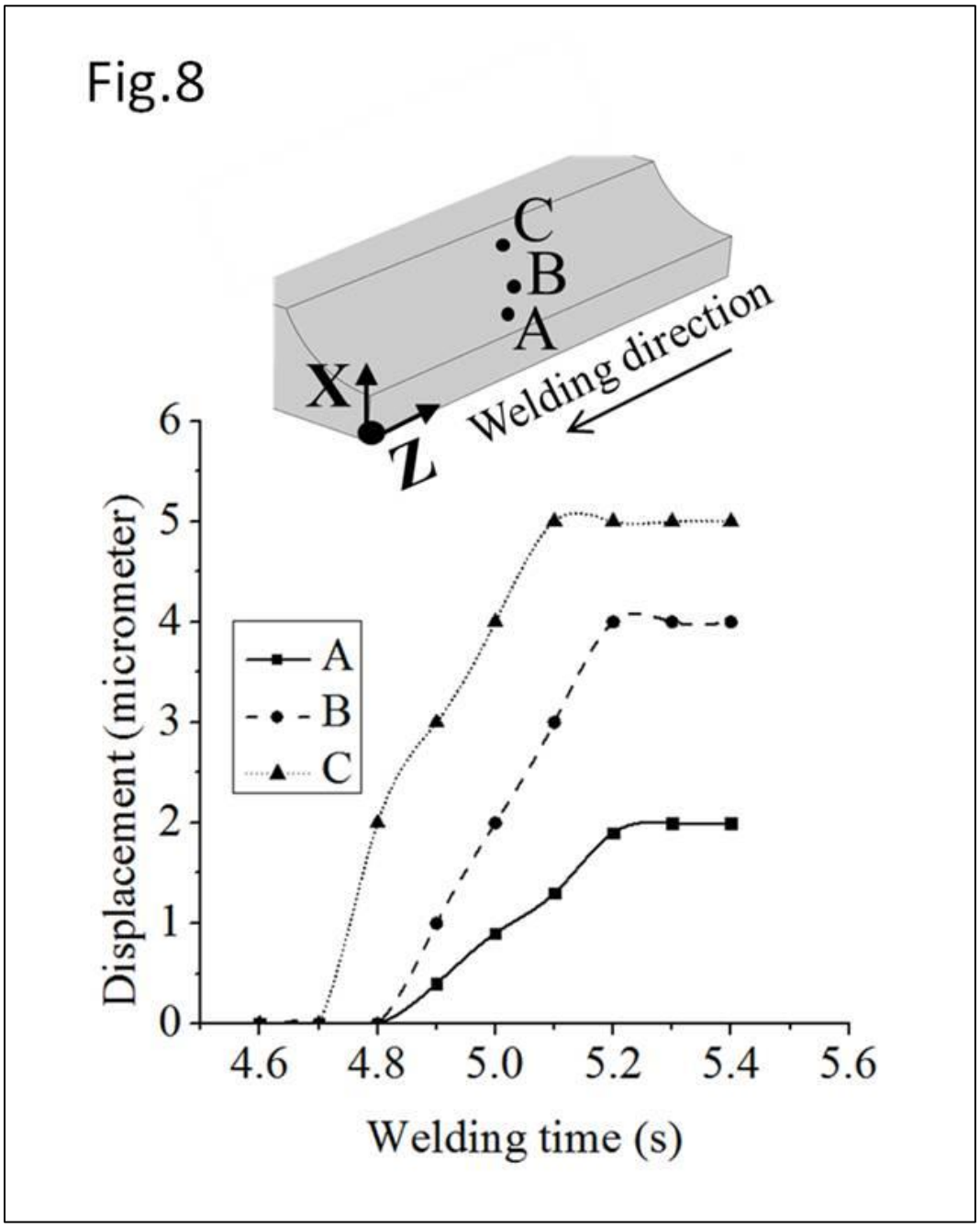

Fig. 9. (a) The lateral components of the force field acting on the fusion surface of the semisolid weld at welding time of t=1.8 s; (b) The corresponding distribution of the solid fraction projected on the fusion surface.

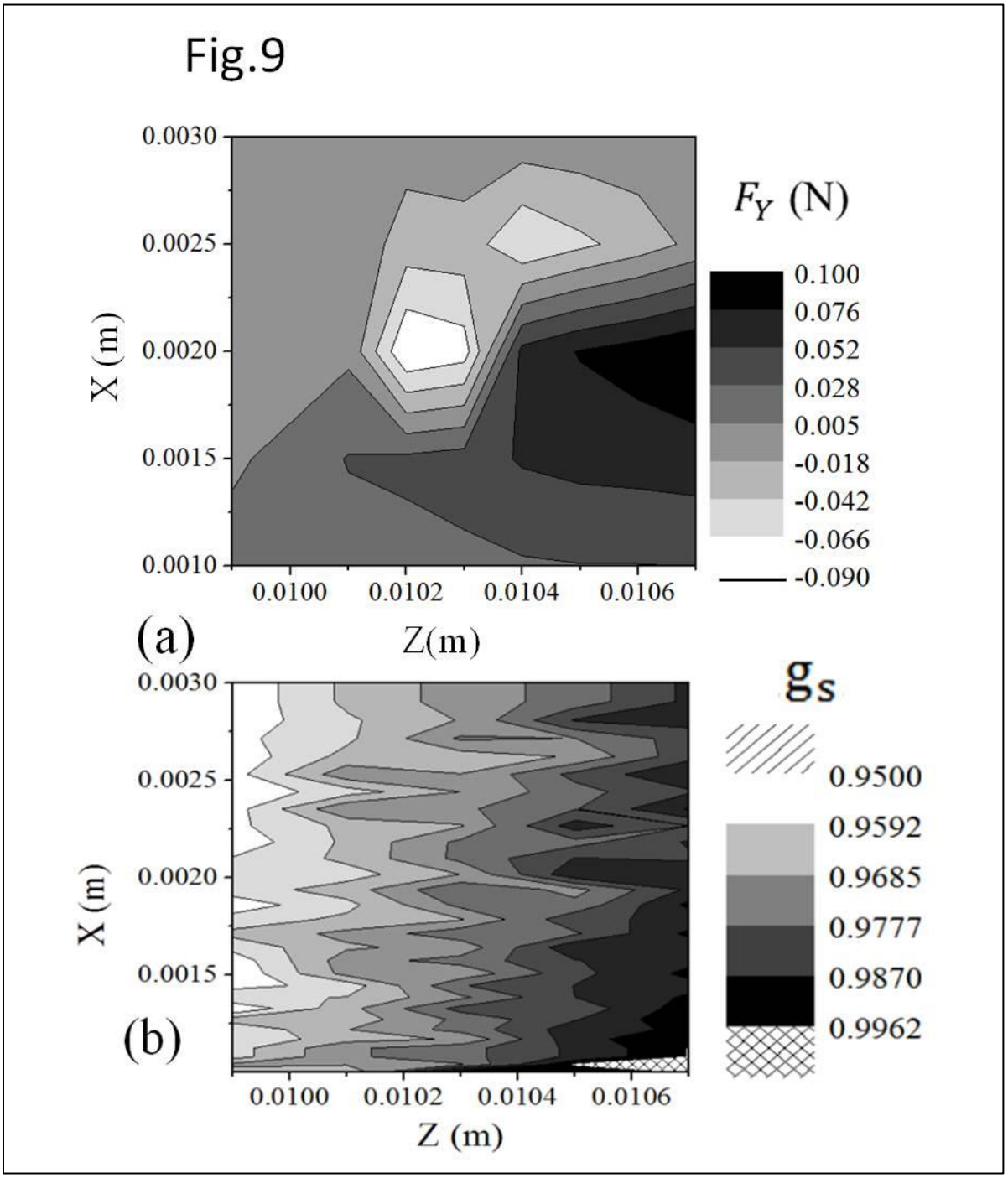

Fig. 10. The calculated average tensile stress for various welding currents at welding speeds of: (a) 2 mm/s; (b) 3mm/s; (c) 4 mm/s; (d) 5 mm/s.

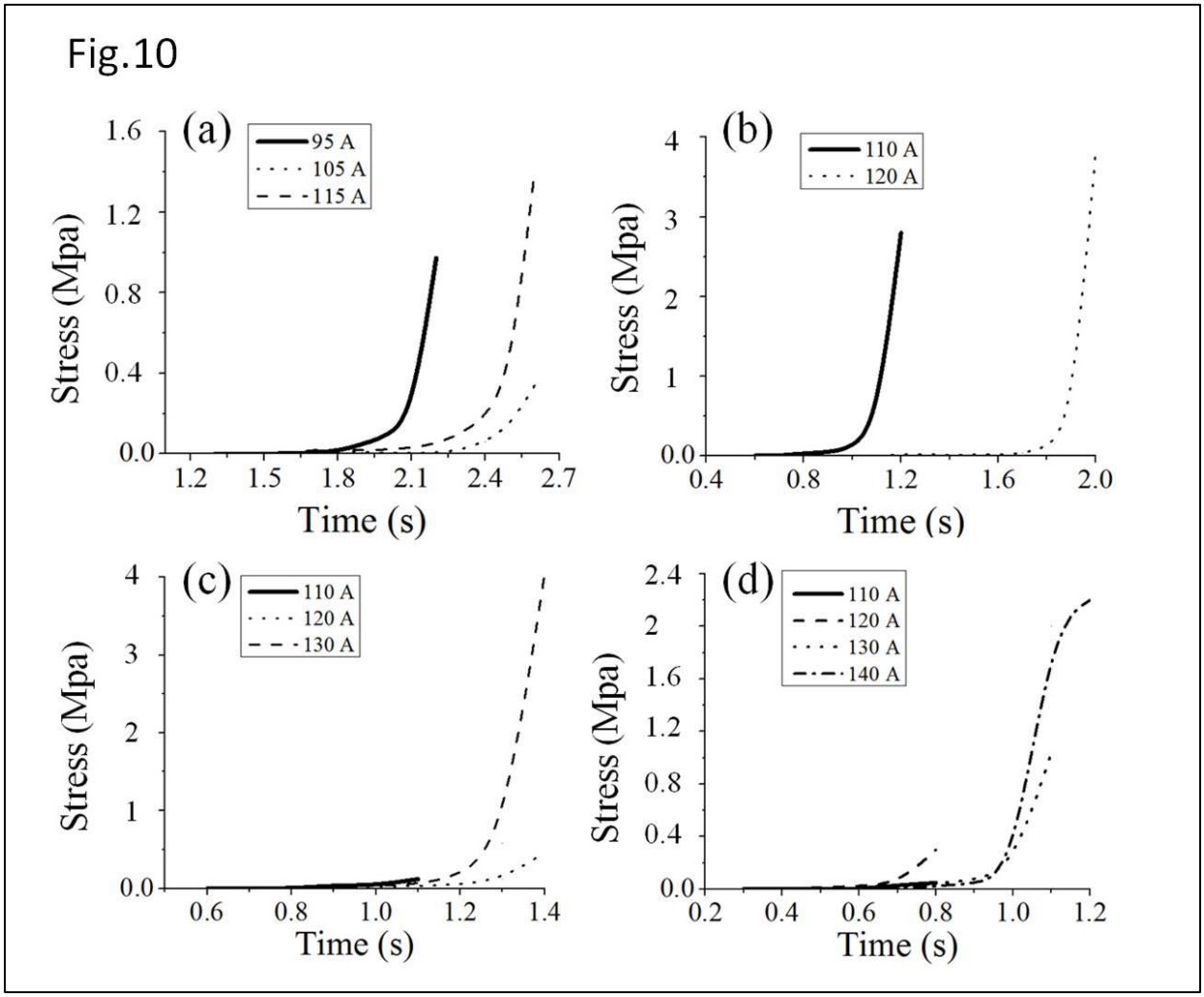

Fig. 11. The variation of the average tensile strain rate during welding of a clamped plate for various welding currents at welding speed of 5 mm/s.

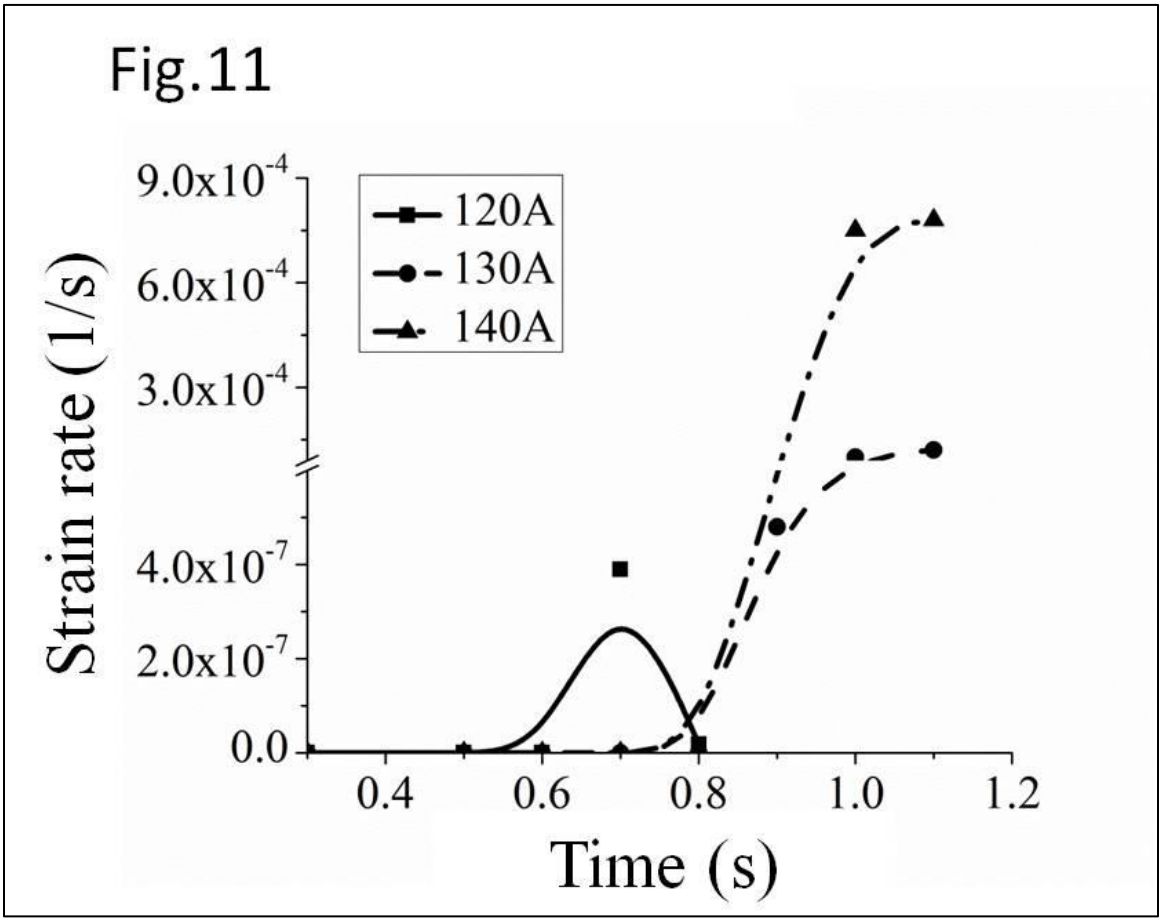

Fig. 12. The average tensile stresses on the weld fusion surface under different constraining conditions.